

## A RAPIDLY SPINNING BLACK HOLE POWERS THE EINSTEIN CROSS

MARK T. REYNOLDS<sup>1</sup>, DOMINIC J. WALTON<sup>2</sup>, JON M. MILLER<sup>1</sup>, AND RUBENS C. REIS<sup>1</sup>

<sup>1</sup> Department of Astronomy, University of Michigan, 311 West Hall, 1085 South University Avenue, Ann Arbor, MI 48109, USA; markrey@umich.edu

<sup>2</sup> Cahill Center for Astronomy and Astrophysics, California Institute of Technology, Pasadena, CA 91125, USA

Received 2014 July 22; accepted 2014 August 7; published 2014 August 20

### ABSTRACT

Observations over the past 20 yr have revealed a strong relationship between the properties of the supermassive black hole lying at the center of a galaxy and the host galaxy itself. The magnitude of the spin of the black hole will play a key role in determining the nature of this relationship. To date, direct estimates of black hole spin have been restricted to the local universe. Herein, we present the results of an analysis of  $\sim 0.5$  Ms of archival *Chandra* observations of the gravitationally lensed quasar Q 2237+305 (aka the “Einstein-cross”), lying at a redshift of  $z = 1.695$ . The boost in flux provided by the gravitational lens allows constraints to be placed on the spin of a black hole at such high redshift for the first time. Utilizing state of the art relativistic disk reflection models, the black hole is found to have a spin of  $a_* = 0.74^{+0.06}_{-0.03}$  at the 90% confidence level. Placing a lower limit on the spin, we find  $a_* \geq 0.65$  ( $4\sigma$ ). The high value of the spin for the  $\sim 10^9 M_\odot$  black hole in Q 2237+305 lends further support to the coherent accretion scenario for black hole growth. This is the most distant black hole for which the spin has been directly constrained to date.

**Key words:** accretion, accretion disks – black hole physics – galaxies: high-redshift – quasars: individual (Q 2237+305) – relativistic processes

*Online-only material:* color figures

### 1. INTRODUCTION

Black holes play a key role in the growth and evolution of galaxies and their stellar content (Fabian 2012). The spin of the black hole ( $a_* \equiv Jc/GM^2$ ) is crucial as it can influence both the radiative and kinetic components of the energy output. In an optically thick, geometrically thin accretion disk, the radiative efficiency, and hence luminosity ( $L = \eta \dot{M} c^2$ ), of the inner region depends on the spin, peaking at  $\eta \gtrsim 0.3$  for a maximal spin black hole ( $a_* \sim 0.998$ ; Thorne 1974). This should be compared to the fiducial spin value estimated from observations of the cosmic X-ray background (CXB;  $\eta \sim 0.1$  or equivalently  $a_* \sim 0.67$ ; Soltan 1982). Similarly, if relativistic jets are powered by tapping the spin of the black hole via, for example, the “Blandford–Znajek” process, a larger spin may result in a more powerful jet ( $P_{\text{jet}} \propto a_*^2 \Phi^2$ , where  $\Phi$  is the magnetic flux; Blandford & Znajek 1977). Hence, the spin distribution of black holes is a crucial ingredient in the feedback process affecting the co-evolution of the black hole and its host galaxy (Fabian 2012).

Direct constraints on the spin of a black hole are now possible via modeling the accretion disk reflection spectrum (Lightman & White 1988; Fabian et al. 1989; Tanaka et al. 1995; Miller 2007). Detailed observations of active galactic nuclei (AGNs) in the local universe ( $z \lesssim 0.1$ ) illustrate the power of this method to constrain the inner accretion flow geometry in the strong gravity regime through both spectral (e.g., Fabian et al. 2009; Risaliti et al. 2013; Reynolds 2013) and timing methods (e.g., Zoghbi et al. 2012; De Marco et al. 2013; Kara et al. 2013; Uttley et al. 2014). However, at present it is only possible to indirectly probe the spin distribution for black holes at high redshift (Davis & Laor 2011; Wu et al. 2013; Trakhtenbrot 2014), though such methods are necessarily hampered by substantial systematic uncertainties, e.g., Raimundo et al. (2012).

In order to determine the influence of the black hole on structure growth, we would like to probe the spin distribution

out to the epoch of peak galaxy and star formation ( $z \sim 2$ ). In Reis et al. (2014), we demonstrated how the boost in flux provided by a strong gravitational lens can be used to constrain the spin of a supermassive black hole (SMBH) lying at a cosmologically relevant distance, i.e., RX J1131–1231 at  $z = 0.658$  ( $\tau_{\text{lookback}} \sim 6$  Gyr). The black hole was found to have a large spin,  $a_* = 0.87^{+0.08}_{-0.15}$  at the  $3\sigma$  confidence level. This is the most distant SMBH for which the spin of the black hole has been directly measured to date. The high spin value would support the coherent accretion scenario (e.g., Volonteri et al. 2013). This source class opens up a promising avenue to begin constraining SMBH spin evolution as a function of redshift and will facilitate comparison with black hole host-galaxy co-evolution models, in particular as models become increasingly sophisticated, e.g., Dubois et al. (2014) and Sesana et al. (2014).

Q 2237+305 was discovered by Huchra et al. (1985) and determined to be a strongly lensed quasar lying at a redshift of  $z = 1.695$ . The quasar is lensed by a Sab-barred galaxy at  $z = 0.0395$  into four distinct components (Yee 1988). Due to the low redshift of the lens, Q 2237+305 commanded immediate interest due to the short interimage time delays ( $\Delta\tau_{\text{ac}}$  is  $\sim 3$  hr) and the discovery of microlensing, which facilitate the detailed study of the quasar and lensing galaxy (see Figure 1; Irwin et al. 1989; Wambsganss & Paczynski 1994). Optical spectroscopy of the gravitationally distorted quasar host galaxy has resulted in the detection of broad and narrow line region components consistent with emission from a typical Seyfert galaxy, e.g., Motta et al. (2004). The black hole has been constrained to have a mass of  $\log_{10} M_{\text{BH}} = 9.08 \pm 0.39 M_\odot$ , based on analysis of the H $\beta$  emission line (Assef et al. 2011). In addition to being quadruply lensed, the quasar flux is also magnified with an average magnification  $\sim 16$  (Schmidt et al. 1998).

The system is of significant interest at X-ray energies as microlensing can provide constraints on the inner accretion flow on scales of astronomical units (Chartas et al. 2012). The quasar is viewed almost face on (Poindexter & Kochanek 2010;

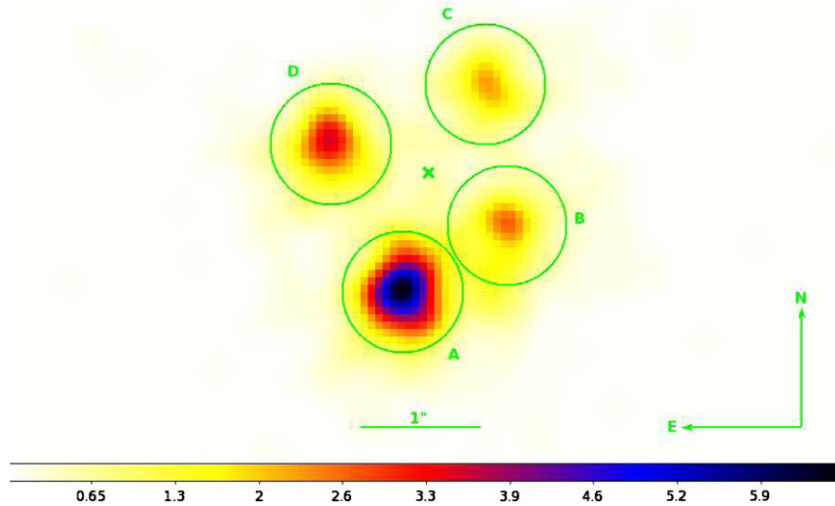


**Figure 1.** Sample *Chandra* image of Q 2237+305 (obsid: 14514) in the 0.35–7.0 keV band, where the four lensed images are clearly resolved. The raw image has been re-binned to one-eighth the native pixel size before smoothing with a Gaussian ( $\sigma = 0''.25$ ). The exposure time is 29.36 ks. The green circles denote our source extraction regions ( $r = 0''.5$ ), while the position of the lensing galaxy ( $z = 0.0395$ ) is marked by the cross.

(A color version of this figure is available in the online journal.)

Sluse et al. 2011). First resolved at X-ray wavelengths by *Chandra*, where, in addition to the detection of an iron K line, a time delay at X-ray energies was also detected ( $\Delta\tau_{\text{ac}} \sim 2.7$  hr; Dai et al. 2003). The microlensing studies have also enabled constraints on the size of the corona, where the source of the hard X-ray emission has been constrained to be compact with a size  $\sim 20 R_g$  or  $\sim 2.9 \times 10^{15}$  cm (Mosquera et al. 2013), and the temperature profile of the accretion disk, which is found to be consistent with expectations from standard thin accretion disk theory, i.e.,  $T(r) \propto r^{-3/4}$ ; Morgan et al. 2010).

In this Letter, we describe analysis of archival *Chandra* observations of Q 2237+305, where we directly measure the spin of the SMBH lying at a redshift of  $z \sim 1.7$ .

## 2. OBSERVATIONS

Our sample consists of 26 observations in total, obtained over the first 13 yr of the operation of *Chandra*, i.e., ut000906–ut130106, where the relevant observation IDs are 00431, 01632, 06831–06840, 11534–11539, 12831, 12832, 13191, 13195, 13960, 13961, 14513, and 14514. Analysis of the majority of these observations have been previously presented in the context of microlensing studies of Q 2237+305 by Dai et al. (2003), Chen et al. (2012), and collaborators. With the exception of the first two observations, which were taken with the standard full frame time of 3.24 s, all subsequent observations were obtained with a frame time of 1.74 s. The summed exposure time is 468 ks.

The analysis procedure follows that undertaken in our analysis of the lensed quasar RX J1131–1231 (Reis et al. 2014). In brief, all data are re-processed in CIAO v4.5<sup>3</sup> utilizing the latest *Chandra* calibration files in the standard manner. Although the individual components of Q 2237+305 are separated by mere arcseconds, the unique spatial resolution of *Chandra* facilitates straightforward imaging of this lensed quasar at X-ray energies. Here, advantage is taken of the native sub-arcsecond spatial resolution provided by the *Chandra* mirrors and now available via the EDSER algorithm in CIAO. All images are re-binned to one-eighth of the native ACIS pixel size before smoothing

with a Gaussian of  $0''.25$ . An example image is displayed in Figure 1. Spectra are extracted from  $0''.5$  radius regions via the SPECEXTRACT script with the point-spread function correction enabled, where the regions are re-centered on each individual component in each image prior to extraction. The overall flux from each individual lensed image from each observation was examined to determine if any of the observations are affected by pile up.<sup>4</sup> Unsurprisingly, given the cosmological distance, pile up does not affect any of the observations considered herein. For completeness, the solitary *XMM-Newton* exposure obtained in 2002 is also considered (Fedorova et al. 2008).

All spectra are subsequently combined using the COMBINE\_SPECTRA script before grouping to a signal-to-noise ratio (S/N) of three per spectral bin with DMGROUP. The spectra and background files are then exported to XSPEC v12.8.0 m<sup>5</sup> for spectral analysis.

## 3. ANALYSIS AND RESULTS

The final summed *Chandra* spectrum contains data from 26 observations with 4 lensed images of the source per observation, resulting in a total on source time of  $\sim 1.8$  Ms. The resulting spectrum contains approximately 22 k net counts in the 0.35–8.0 keV energy range. Data outside this interval are not considered further due to low S/N and/or high backgrounds.

Initially, the brightest source image in each observation was characterized with a simple power law in order to search for evidence of extreme microlensing variability, which can affect the Fe K region by, for example, introducing narrow redshifted Fe line components to the spectrum, such as that previously observed in RX J1131–1231 (Chartas et al. 2012). The brightest image does not reveal any evidence for any anomalous variability; however, we note that the S/N is necessarily low in individual exposures.

Our energy range of interest, 0.35–8 keV, corresponds to the energy range 0.94–21.56 keV in the quasar rest frame, thus providing access to the Fe K line and a portion of the Compton hump region of the reflection spectrum.

<sup>3</sup> <http://cxc.harvard.edu/ciao>

<sup>4</sup> [http://cxc.harvard.edu/ciao/download/doc/pileup\\_abc.pdf](http://cxc.harvard.edu/ciao/download/doc/pileup_abc.pdf)

<sup>5</sup> <http://heasarc.gsfc.nasa.gov/xanadu/xspec/>

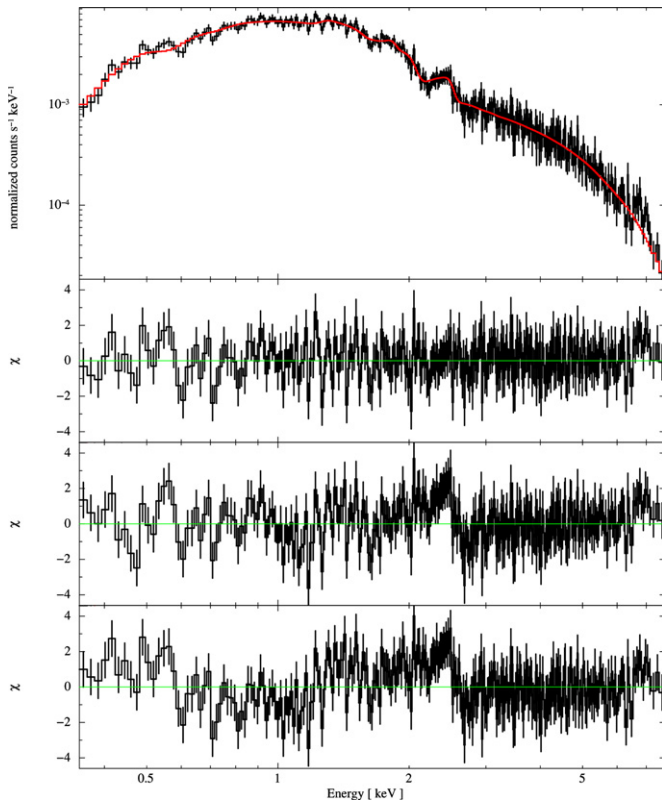


**Figure 2.** Our initial phenomenological fit to the combined data. The final best-fit model is a combination of a power law, a disk component representing the “soft excess”, and a broad relativistically skewed iron line, i.e., `pha(zpha(diskbb+po+relline))`. The residuals to the best-fit model are displayed below the upper panel and represent, from bottom to top, a single power law, a power law plus disk, and a disk plus line plus power law. The best-fit spin returned by this model is  $a_* = 0.75 \pm 0.03$  at the 90% confidence level.

(A color version of this figure is available in the online journal.)

To characterize the spectrum, we fit the data with a simple power law modified by absorption in the Galaxy and the lens, i.e., `pha(zpha(zpo))`<sup>6</sup>, where  $N_{H,\text{local}} = 0.05 \times 10^{22} \text{ cm}^{-2}$  and  $N_{H,\text{lens}} \sim 0.1 \times 10^{22} \text{ cm}^{-2}$  (Dai et al. 2003). This fit reveals characteristic residuals consistent with those expected from the soft excess at lower energies ( $\lesssim 1 \text{ keV}$ ) and a broad iron line at a rest-frame energy of  $\sim 6.4 \text{ keV}$ ; see Figure 2. In the standard manner, we initially characterize the properties of the observed residuals using simple models, e.g., see Reis et al. (2014).

The soft excess is accounted for using a `diskbb` component. Fitting the broad line component with a Gaussian reveals a broad line ( $\text{EW} = 167^{+48}_{-42} \text{ eV}$ ,  $\sigma = 0.52 \pm 0.14 \text{ keV}$ ) whose centroid energy is skewed to lower energies ( $E_{\text{line}} = 6.05^{+0.20}_{-0.17} \text{ keV}$ ), as it attempts to account for the red wing of what is in fact a relativistically broadened line. To more accurately model this line, we utilize the relativistic line model `relline` of Dauser et al. (2010). The final phenomenological model (`pha(zpha(diskbb+po+relline))`) provides an excellent fit to the data ( $\chi^2/\nu = 368/339$ ), as is evidenced in Figure 2. Of particular note, the `relline` component suggests a rapidly spinning black hole viewed at low inclination, i.e.,  $a_* = 0.76 \pm 0.03$ ,  $E_{\text{line}} = 6.82^{+0.12}_{-0.09} \text{ keV}$ ,  $q_{\text{in}} \geq 6.63$ ,  $r_{\text{break}} = 4.36^{+0.45}_{-0.31} R_g$ ,  $q_{\text{out}} = 3.12^{+0.20}_{-0.26}$ , and  $i \leq 13^\circ 08'$ , where

**Table 1**  
Best-fit Model Parameters

Parameter	$Z_{\text{Fe}} \equiv Z_{\odot}$	$Z_{\text{Fe}} \text{ Variable}$
$N_{H,\text{local}} (10^{22} \text{ cm}^{-2})$	0.05	0.05
$N_{H,\text{lens}} (10^{22} \text{ cm}^{-2})$	$(0.11 \pm 0.01)$	$(0.06 \pm 0.01)$
$E_{\text{line}} (\text{keV})$	$6.58 \pm 0.03$	$6.58^{+0.02}_{-0.06}$
$\text{Norm}_{\text{line}}$	$(6.6 \pm 2.9) \times 10^{-7}$	$(6.6 \pm 3.1) \times 10^{-7}$
$\Gamma$	$1.80^{+0.16}_{-0.11}$	$1.64 \pm 0.04$
$\text{Norm}_{\text{po}}$	$(3.9^{+1.6}_{-1.8}) \times 10^{-5}$	$(7.8 \pm 0.08) \times 10^{-5}$
$q_{\text{in}}$	$\geq 7.6$	$\geq 7.3$
$q_{\text{out}}$	$3.02 \pm 0.25$	$3.31 \pm 0.28$
$r_{\text{break}} (R_g)$	$4.65^{+0.48}_{-0.32}$	$4.35^{+0.59}_{-0.26}$
$i (^\circ)$	$\leq 11.5$	$\leq 11.7$
$a_*$	$0.73^{+0.05}_{-0.02}$	$0.74^{+0.06}_{-0.03}$
$\xi (\text{erg cm s}^{-1})$	$681^{+339}_{-139}$	$993^{+155}_{-378}$
$Z_{\text{Fe}} [Z_{\odot}]$	1.0	$\geq 6.2$
$\text{Norm}_{\text{reflionx}}$	$(8.5^{+7.1}_{-1.4}) \times 10^{-9}$	$(2.8^{+4.5}_{-1.1}) \times 10^{-9}$
...	...	...
$R_{\text{frac}}$	$2.4^{+2.8}_{-1.0}$	$0.40 \pm 0.12$
$L_{2-10 \text{ keV}} (\text{erg s}^{-1})$	$(1.26^{+0.95}_{-0.14}) \times 10^{45}$	$(1.27^{+0.13}_{-0.54}) \times 10^{45}$
...	...	...
$\chi^2/\nu$	388/339	371/338

**Notes.** Parameters of our best-fit model: `pha(zpha(zpo+zgauss+relconv*reflionx))`. Galactic absorption and absorption in the low-redshift lensing galaxy are included. The reflection fraction is defined as  $R_{\text{frac}} \equiv F_{\text{refl}}/F_{\text{illum}}$ , where the unabsorbed fluxes are calculated in the 0.1–100 keV band (observed frame) by extrapolation of the best-fit model. The 2–10 keV rest-frame luminosity is calculated via the `lumin` command assuming  $z = 1.695$ ,  $H_0 = 70 \text{ km s}^{-1} \text{ Mpc}^{-1}$ ,  $\Omega_{\Lambda} = 0.73$ . All parameters are quoted with errors at the 90% confidence level.

all of the errors are at the 90% confidence level. The low inclination returned by the model agrees with previous work suggesting the quasar is viewed approximately face on (Poindexter & Kochanek 2010; Sluse et al. 2011). The radial emissivity profile of the reflected emission is parameterized by a broken power law, where the large inner index is consistent with preferentially beamed emission from a compact corona, lying at small separation from the black hole, onto the inner disk due to a rapidly spinning black hole, e.g., see Wilkins & Fabian (2012).

Given the clear presence of reflection signatures in the spectrum, we now proceed to apply a self-consistent disk reflection model in combination with a state of the art relativistic convolution kernel: `relconv` and `reflionx` (Dauser et al. 2010; Ross & Fabian 2005). Our final model is `pha(zpha(zpo + zgauss + relconv*reflionx))`.<sup>7</sup> As this model is physically self-consistent, an additional narrow Gaussian line is required to fit the observed line profile ( $E_{\text{line}} \sim 6.6 \text{ keV}$ ,  $\text{EW} \sim 40 \text{ eV}$ ); see Figure 3. This differs from the simple model above where the `relline` component is free to fit the data without knowledge of the broader continuum. Nonetheless, the parameters of the inner accretion flow are remarkably similar to the phenomenological model, i.e.,  $a_* = 0.73^{+0.05}_{-0.02}$  (90% confidence level). This model is reflection-dominated,  $R_{\text{frac}} = 2.8^{+2.8}_{-1.0}$ , where the reflection fraction is defined  $R_{\text{frac}} \equiv F_{\text{refl}}/F_{\text{illum}}$ ; see Table 1 for details.

The solar abundance model is of slightly lower quality in comparison to the phenomenological model presented earlier, with evidence of systematic residuals at low energy (compare Figures 2 and 3). Enhanced iron abundances have been discovered in the inner accretion disk for a number of AGNs,

<sup>6</sup> The abundance model of Asplund et al. (2009) is used throughout this work, i.e., `aspl`.

<sup>7</sup> Our results using the `reflionx` reflection tables were compared to similar fits using the recent `xillver` reflection tables of García et al. (2013), and were found to be consistent within the quoted errors.



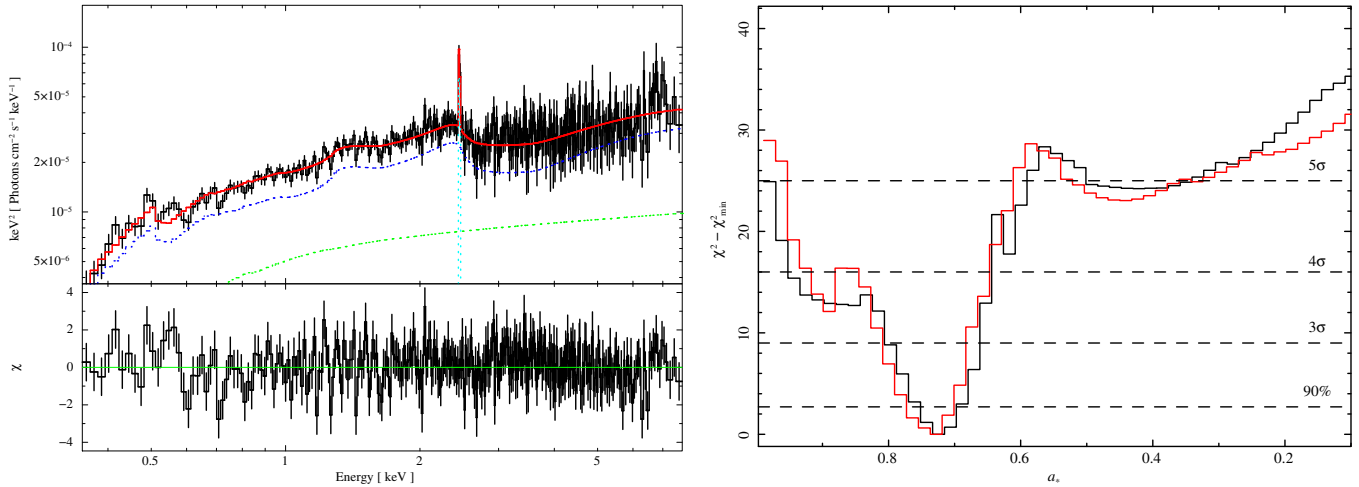


**Figure 3.** Left: final best-fit solar abundance self-consistent relativistic reflection model (`pha(zpha(zpo+zgauss+relconv*reflionx))`) to the summed *Chandra* spectrum of Q 2237+305 with residuals. The illuminating power law is indicated in green, the reflected emission in blue, and the narrow Fe K line in cyan, with the sum indicated in red. The black hole is determined to be rapidly spinning, i.e.,  $a_* = 0.73^{+0.05}_{-0.02}$  at the 90% confidence level. Right: contour plot of the spin parameter ( $a_*$ ) calculated via the `steppar` command, for the reflection model plotted on the left (black:  $\chi^2_{\min} = 388$ ) and for a similar model with a variable iron abundance (red:  $\chi^2_{\min} = 371$ ). The 90%, 3 $\sigma$ , 4 $\sigma$ , and 5 $\sigma$  confidence intervals are indicated by the dashed lines, demonstrating the robust nature of the spin constraint, i.e.,  $a_* \geq 0.65(4\sigma)$ ; see Table 1 for the best-fit parameters.

(A color version of this figure is available in the online journal.)

e.g., Fabian et al. (2009) and Risaliti et al. (2013). As such, the above model is re-fit with a variable iron abundance ( $\Delta\chi^2/\Delta\nu = 17$ ). This model is qualitatively similar to the solar abundance model; see Table 1. However, the enhanced reflection component in the iron band results in a modified continuum requiring a mildly harder illuminating power law ( $\Gamma \sim 1.6$ ) and commensurately higher ionization of the accretion disk ( $\xi \sim 10^3 \text{ erg cm s}^{-1}$ ). The iron abundance is large,  $Z_{\text{Fe}} \geq 6.2 Z_{\odot}$  (90%), reducing to  $\sim 3.8 Z_{\odot}$  at the 3 $\sigma$  confidence level. In Figure 3 (right), we plot confidence contours of the spin parameter for both models. It is clear that our ability to constrain the spin is robust with respect to our ability to constrain the Fe abundance.

The 2–10 keV rest-frame luminosity is measured to be  $L_x \sim 1.3 \times 10^{45} \text{ erg s}^{-1}$  (Table 1). Given that the bolometric correction and the magnification of this quasar work in the opposite sense and likely have similar magnitudes (within a factor of two, i.e., Schmidt et al. 1998; Vasudevan & Fabian 2007), this luminosity corresponds to a relatively low Eddington rate of  $\sim 0.01 L_{\text{Edd}}(10^9 M_{\odot}/M)$ .

Finally, we note that the above model was also applied to the single existing *XMM-Newton* observation (Fedorova et al. 2008). This observation resulted in only  $\sim 12$  ks goodtime with EPIC/pn and  $\sim 20$  ks for each of the MOS CCDs. The S/N in this observation is low, containing only  $\sim 2000$  counts in the EPIC/pn exposure, and  $\sim 1000$  with each MOS camera. Nonetheless, the spectrum is consistent with the reflection spectrum detected by *Chandra* at higher S/N discussed above. As such, we do not consider this data set further.

#### 4. DISCUSSION

In this Letter, we present a direct measurement of the spin of the black hole at high redshift, i.e.,  $\tau_{\text{lookback}} \sim 10 \text{ Gyr}$ . This is the most distant black hole for which a direct constraint on the spin has been made to date. The spin of the black hole in the quasar Q 2237+305 is found to be  $a_* \geq 0.65$  at the 4 $\sigma$  confidence level. Thus, the Q 2237+305 SMBH is rapidly rotating during the epoch of peak star formation and

galaxy growth. Models for the spin evolution of a growing SMBH predict the largest differences for the most massive black holes ( $M_{\text{BH}} \gtrsim 10^9 M_{\odot}$ , e.g., Volonteri et al. 2013). As a probe of SMBH/galaxy co-evolution, the measured high spin for the black hole in Q 2237+305 would support the coherent accretion scenario for black hole growth. It is also noteworthy that the high measured value for the spin implies an accretion efficiency consistent with or greater than that implied by the Soltan argument (Soltan 1982).

Our analysis is necessarily aggressive given the moderate number of counts available. However, the theoretical and observational support for the reflection model utilized herein has considerable support from an increasing number of high S/N ratio observations at low redshift, e.g., Fabian et al. (2009), Zoghbi et al. (2012), De Marco et al. (2013), Risaliti et al. (2013), Kara et al. (2013), and Walton et al. (2014). The best-fit reflection model requires an enhanced iron abundance ( $Z_{\text{Fe}} \geq 3.8 Z_{\odot}$  (3 $\sigma$ ); see Table 1). Such a large iron abundance in the inner accretion flow has been observed in a number of local universe AGNs, e.g., 1H0707-495 (Fabian et al. 2009), NGC 1365 (Risaliti et al. 2013), and in larger samples of systems (Walton et al. 2013).

The enhanced iron abundance is required by the presence of residuals at low energies, i.e.,  $\lesssim 1 \text{ keV}$  in the observer frame. This corresponds to rest-frame energies  $\lesssim 2.7 \text{ keV}$ . Such residuals can, in principle, originate in an absorption component (Miller et al. 2008), though a large column would be required to effect emission at such high energies. This possibility was investigated by the addition of a partial covering absorber to the solar abundance model, i.e., `pha(zpha(zpcfabs(zpo+zgauss+relconv*reflionx)))`. The improvement in the fit is similar to the variable abundance model but with an extra degree of freedom ( $\Delta\chi^2/\Delta\nu = 15/2$ ). The column density is large as expected,  $N_{\text{H}} \sim 10^{23} \text{ cm}^{-2}$ , and a covering fraction  $f_{\text{cov}} \sim 0.3$ . This model requires a soft power-law index of  $\Gamma \sim 2$ . This model is disfavored for a number of reasons: (1) optical studies of Q 2237+305 find the extinction to be modest ( $0.8 \lesssim A_V \lesssim 1.2$ ; Agol et al. 2000) and consistent with the small X-ray column, i.e.,  $N_{\text{H}} \sim 10^{21} \text{ cm}^{-2}$  (Dai et al. 2003); (2) optically thick winds are unlikely to form

in the inner disks of AGNs at the luminosity observed herein ( $L_x \lesssim 0.01 L_{\text{Edd}}$ , Reynolds 2012); and (3) the recent *NuStar* observations of low-redshift AGNs, which have demonstrated the broadband spectrum to be consistent with the reflection scenario, e.g., Risaliti et al. (2013) and Walton et al. (2014).

Q 2237+305 is the second high-redshift quasar that we have been able to measure the spin of by taking advantage of the boost in flux provided by a strong gravitational lens. Previously, the spin of the  $\log_{10} M_{\text{BH}} \sim 8.3 M_{\odot}$  SMBH in the  $z = 0.658$  quasar RX J1131–1231 has been determined to be  $a_* = 0.87^{+0.08}_{-0.15}$  (Reis et al. 2014), also consistent with the coherent accretion scenario.

Models for black hole growth and evolution and their co-evolution with the host galaxy are becoming more sophisticated, e.g., Dubois et al. (2014) and Sesana et al. (2014). However, it is important to note that caution is required in interpreting these observational results at the current time. Besides the small size of the sample, the quasars for which this type of study will be possible do not form a statistically complete sample and as such may be subject to considerable bias, e.g., we could be sampling the most luminous systems as the luminosity of the accretion flow will have a spin dependence with larger spins facilitating more luminous inner accretion flows.

Finally, we note that quasars are known to be a major contributor to the CXB, as such knowledge of the precise form of their spectral energy distribution is important (Ueda et al. 2014). The reflection contribution to the X-ray spectrum of Q 2237+305 is uncertain primarily due to our inability to accurately constrain the iron abundance in the current observation, i.e.,  $0.5 \lesssim R_{\text{frac}} \lesssim 2.5$  (see Table 1). Further observations will be required in order to constrain the iron abundance and hence the reflection fraction of this high-redshift black hole.

We extend our thanks to the anonymous referee. This research has made use of *Chandra* data obtained from *HEASARC*. This research made extensive use of NASA's Astrophysics Data System.

## REFERENCES

- Agol, E., Jones, B., & Blaes, O. 2000, *ApJ*, **545**, 657  
 Asplund, M., Grevesse, N., Sauval, A. J., & Scott, P. 2009, *ARA&A*, **47**, 481  
 Assef, R. J., Denney, K. D., Kochanek, C. S., et al. 2011, *ApJ*, **742**, 93  
 Blandford, R. D., & Znajek, R. L. 1977, *MNRAS*, **179**, 433  
 Chartas, G., Kochanek, C. S., Dai, X., et al. 2012, *ApJ*, **757**, 137  
 Chen, B., Dai, X., Kochanek, C. S., et al. 2012, *ApJ*, **755**, 24  
 Dai, X., Chartas, G., Agol, E., Bautz, M. W., & Garmire, G. P. 2003, *ApJ*, **589**, 100  
 Dauser, T., Wilms, J., Reynolds, C. S., & Brenneman, L. W. 2010, *MNRAS*, **409**, 1534  
 Davis, S. W., & Laor, A. 2011, *ApJ*, **728**, 98  
 De Marco, B., Ponti, G., Cappi, M., et al. 2013, *MNRAS*, **431**, 2441  
 Dubois, Y., Volonteri, M., & Silk, J. 2014, *MNRAS*, **440**, 1590  
 Fabian, A. C. 2012, *ARA&A*, **50**, 455  
 Fabian, A. C., Rees, M. J., Stella, L., & White, N. E. 1989, *MNRAS*, **238**, 729  
 Fabian, A. C., Zoghbi, A., Ross, R. R., et al. 2009, *Natur*, **459**, 540  
 Fedorova, E. V., Zhdanov, V. I., Vignali, C., & Palumbo, G. G. C. 2008, *A&A*, **490**, 989  
 García, J., Dauser, T., Reynolds, C. S., et al. 2013, *ApJ*, **768**, 146  
 Huchra, J., Gorenstein, M., Kent, S., et al. 1985, *AJ*, **90**, 691  
 Irwin, M. J., Webster, R. L., Hewett, P. C., Corrigan, R. T., & Jedrzejewski, R. I. 1989, *AJ*, **98**, 1989  
 Kara, E., Fabian, A. C., Cackett, E. M., et al. 2013, *MNRAS*, **434**, 1129  
 Lightman, A. P., & White, T. R. 1988, *ApJ*, **335**, 57  
 Miller, J. M. 2007, *ARA&A*, **45**, 441  
 Miller, L., Turner, T. J., & Reeves, J. N. 2008, *A&A*, **483**, 437  
 Morgan, C. W., Kochanek, C. S., Morgan, N. D., & Falco, E. E. 2010, *ApJ*, **712**, 1129  
 Mosquera, A. M., Kochanek, C. S., Chen, B., et al. 2013, *ApJ*, **769**, 53  
 Motta, V., Mediavilla, E., Muñoz, J. A., & Falco, E. 2004, *ApJ*, **613**, 86  
 Poindexter, S., & Kochanek, C. S. 2010, *ApJ*, **712**, 668  
 Raimundo, S. I., Fabian, A. C., Vasudevan, R. V., Gandhi, P., & Wu, J. 2012, *MNRAS*, **419**, 2529  
 Reis, R. C., Reynolds, M. T., Miller, J. M., & Walton, D. J. 2014, *Natur*, **507**, 207  
 Reynolds, C. S. 2012, *ApJL*, **759**, L15  
 Reynolds, C. S. 2013, SSRv, (arXiv:1302.3260)  
 Risaliti, G., Harrison, F. A., Madsen, K. K., et al. 2013, *Natur*, **494**, 449  
 Ross, R. R., & Fabian, A. C. 2005, *MNRAS*, **358**, 211  
 Schmidt, R., Webster, R. L., & Lewis, G. F. 1998, *MNRAS*, **295**, 488  
 Sesana, A., Barausse, E., Dotti, M., & Rossi, E. M. 2014, arXiv:1402.7088  
 Sluse, D., Schmidt, R., Courbin, F., et al. 2011, *A&A*, **528**, A100  
 Soltan, A. 1982, *MNRAS*, **200**, 115  
 Tanaka, Y., Nandra, K., Fabian, A. C., et al. 1995, *Nature*, **375**, 659  
 Thorne, K. S. 1974, *ApJ*, **191**, 507  
 Trakhtenbrot, B. 2014, *ApJL*, **789**, L9  
 Ueda, Y., Akiyama, M., Hasinger, G., Miyaji, T., & Watson, M. G. 2014, *ApJ*, **786**, 104  
 Uttley, P., Cackett, E. M., Fabian, A. C., Kara, E., & Wilkins, D. R. 2014, arXiv:1405.6575  
 Vasudevan, R. V., & Fabian, A. C. 2007, *MNRAS*, **381**, 1235  
 Volonteri, M., Sikora, M., Lasota, J.-P., & Merloni, A. 2013, *ApJ*, **775**, 94  
 Walton, D. J., Nardini, E., Fabian, A. C., Gallo, L. C., & Reis, R. C. 2013, *MNRAS*, **428**, 2901  
 Walton, D. J., Risaliti, G., Harrison, F. A., et al. 2014, *ApJ*, **788**, 76  
 Wambsganss, J., & Paczynski, B. 1994, *AJ*, **108**, 1156  
 Wilkins, D. R., & Fabian, A. C. 2012, *MNRAS*, **424**, 1284  
 Wu, S., Lu, Y., Zhang, F., & Lu, Y. 2013, *MNRAS*, **436**, 3271  
 Yee, H. K. C. 1988, *AJ*, **95**, 1331  
 Zoghbi, A., Fabian, A. C., Reynolds, C. S., & Cackett, E. M. 2012, *MNRAS*, **422**, 129